

Femtosecond dynamics and laser control of charge transport in *trans*-polyacetylene

Ignacio Franco,¹ Moshe Shapiro,² and Paul Brumer¹

¹*Chemical Physics Theory Group, Department of Chemistry, and Center for Quantum Information and Quantum Control, University of Toronto, Toronto, Ontario, Canada.*

²*Chemical Physics Department, The Weizmann Institute, Rehovot, Israel, and Departments of Chemistry and Physics, The University of British Columbia, Vancouver, B.C., Canada*

(Dated: October 31, 2018)

The induction of dc electronic transport in rigid and flexible *trans*-polyacetylene oligomers according to the ω vs. 2ω coherent control scenario is investigated using a quantum-classical mean field approximation. The approach involves running a large ensemble of mixed quantum-classical trajectories under the influence of $\omega + 2\omega$ laser fields, and choosing the initial conditions by sampling the ground-state Wigner distribution function for the nuclei. The vibronic couplings are shown to change the mean single-particle spectrum, introduce ultrafast decoherence, and enhance intramolecular vibrational and electronic relaxation. Nevertheless, even in the presence of significant couplings, limited coherent control of the electronic dynamics is still viable, the most promising route involving the use of fs pulses with a duration that is comparable to the electronic dephasing time. The simulations offer a realistic description of the behavior of a simple coherent control scenario in a complex system, and provide a detailed account of the femtosecond photoinduced vibronic dynamics of a conjugated polymer.

I. INTRODUCTION

Conjugated polymers are of interest for their broad technological applications [1, 2, 3] and because they are model systems that offer insight into the properties of soft organic and biological matter. As almost every photochemical, photophysical, spectroscopic and charge and energy transfer process in these materials involves dynamics of photoexcited states, the possibility to manipulate, at a molecular level, the dynamical properties of these excitations by means of lasers with well defined phases may have profound technological implications.

As a first step toward this goal, we are interested in manipulating the dynamics of photoexcited electrons along the backbone of a conjugated polymer using the principles of coherent control [4]. Specifically, we want to induce net dipoles along the material without introducing a bias voltage. For this we apply zero-mean laser pulses with frequency components ω and 2ω . Such fields are known to induce phase-controllable dipoles or currents in anharmonic symmetric systems [5] even when they have a zero-temporal mean, a phenomenon that is referred to as laser-induced symmetry breaking. This rectification effect first appears in the third order nonlinear response of the system to the radiation field [6]. At this order the system mixes the frequencies and harmonics of the $\omega + 2\omega$ field, generating a phase-controllable zero harmonic (DC) component in the response. The DC component in the photoinduced dipoles is typically of the form $\langle \mu \rangle \sim \epsilon_{\omega}^2 \epsilon_{2\omega} \cos(\phi_{2\omega} - 2\phi_{\omega})$, where $\epsilon_{n\omega}$ and $\phi_{n\omega}$ denote the amplitude and phase of the $n\omega$ component of the field. Hence, simply by varying the relative phase between the two incident lasers one can exert control over the magnitude and sign of the symmetry breaking.

Laser-induced symmetry breaking [4, 6] has been

demonstrated in a wide variety of systems ranging from atoms to solid state samples. Experimentally, it has been implemented for generating anisotropy in atomic photoionization [7], photocurrents in quantum wells [8], intrinsic semiconductors [9] and metal surfaces [10], as well as directed diffusion in symmetric optical lattices [11]. Theoretically, it has been studied for generating transport in doped [12] and bulk semiconductors through interband [13] and intraband [14] excitations, in graphene and carbon nanosheets [15] and in molecular wires [16, 17, 18], among others. The setup is of interest since, with current laser technology, it can be employed to generate controlled transport on a femtosecond timescale.

Of major concern when using lasers to generate electronic transport is the influence of the lattice dynamics on the rectification. The lattice can induce ultrafast dephasing [19, 20] processes that have deleterious effects on the control. Only a few attempts to quantify this effect exist. In all of them, the explicit dependence of the dynamics on the nuclear degrees of freedom is eliminated, and the effect of the lattice has been modeled through phenomenological relaxation [9], stochastic forces [14] or thermal baths [18]. Although formulations of this type have a considerable domain of applicability, they are not appropriate here since the electronic dynamics and spectroscopic observables in conjugated polymers depend on the detailed dynamics of the molecular backbone [21, 22, 23]. This coupling between, and mutual influence of, electronic and vibrational degrees of freedom gives rise to the very rich photophysics of solitons, polarons and breathers and constitutes an important distinction between “soft” materials and rigid solids [1, 22, 24]. Furthermore, the constant exchange of energy between the electronic and nuclear degrees of freedom during photoexcitation keeps the vibrations out

of equilibrium, rendering the thermal description inappropriate.

Here we numerically investigate the effect of vibronic couplings on the applicability of laser-induced symmetry breaking in π -conjugated systems by explicitly following the dynamics of both electronic and vibrational degrees of freedom. The simulations presented below provide a realistic description of the behavior of a simple laser control scenario in a complex system, and offer a detailed account of the femtosecond vibronic dynamics of a conjugated polymer.

As a minimal microscopic model for conjugated polymers we adopt the Su-Schrieffer-Heeger (SSH) Hamiltonian for *trans*-polyacetylene (PA) [1, 24]. The SSH model treats the polymer chain in terms of a one-dimensional tight-binding model in which the π electrons are coupled to distortions in the polymer backbone by electron-vibrational interactions. It neglects quasiparticles interactions, assuming that they are relatively weak due to screening. Despite of its simplicity, the SSH Hamiltonian has been remarkably successful in reproducing the band structure and the dynamics of excitations in PA. With it, we follow numerically the highly nonlinear coupled dynamics of electronic and vibrational degrees of freedom in neutral PA chains during and after photoexcitation with $\omega + 2\omega$ laser pulses of varying frequency, width and intensity. The simulations are performed in a mean-field (Ehrenfest) approximation [25, 26, 27, 28] in which the nuclei are treated classically and the electrons quantum mechanically. Mean-field dynamics is the simplest mixed quantum-classical method that allows transfer of energy between quantum and classical coordinates with a proper conservation of energy [25, 26, 27, 28], and where transitions between instantaneous eigenstates are allowed. Allowing for change in the occupation of the electronic levels is crucial because the laser is constantly inducing electronic transitions and, additionally, electronic levels can approach one another closely during the dynamics and may lead to nonadiabatic transitions between electronic states. It is also a tractable method, as shown below, for treating the vibronic dynamics of multiple electronic states in the presence of a laser.

In order to incorporate the effects of lattice fluctuations on the dynamics we follow the evolution of an ensemble of quantum-classical trajectories. The initial conditions are obtained by using importance sampling for the nuclear Wigner phase space distribution in the harmonic approximation. In this way, the resulting averaged dynamical observables retain relevant correlations between the electronic and vibrational degrees of freedom and are subject to electron-vibrational induced decoherence and relaxation.

This analysis begins by briefly describing the model Hamiltonian (Sec. II A) and deriving the equations of motion for the vibronic dynamics (Sec. II B). Then we turn to the important problem of choosing initial conditions for the evolution (Sec. II C) and we introduce the geometric and spectroscopic observables that are used

to monitor the dynamics (Sec. II D). Our main results are presented in Sec. III. Specifically, after discussing the properties of the initial state (Sec. III A), we investigate the typical dynamics of the chain generated by short (10 fs) and long (300 fs) pulses, and estimate the typical electronic dephasing times in PA oligomers (Sec. III B). Then, we turn our attention to the effects that the lattice dynamics has on laser-induced symmetry breaking (Sec. III C). The main results are summarized in Sec. IV.

II. MODEL AND METHODS

A. The SSH model

The SSH Hamiltonian [1, 24] models the PA oligomer as a one-dimensional tight-binding chain, each site representing a CH unit. The Hamiltonian for an N -membered chain has the form:

$$H_{\text{SSH}} = H_{\pi} + H_{\pi\text{-ph}} + H_{\text{ph}}, \quad (1)$$

where

$$H_{\pi} = -t_0 \sum_{n=1}^{N-1} \sum_{s=\pm 1} (c_{n+1,s}^{\dagger} c_{n,s} + c_{n,s}^{\dagger} c_{n+1,s}), \quad (2)$$

describes the hopping of π electrons along the chain without spin flip characterized by the lowest-order hopping integral t_0 . The operator $c_{n,s}^{\dagger}$ ($c_{n,s}$) creates (annihilates) a fermion in site n with spin s and satisfies the usual fermionic anticommutation relations $\{c_{n,s}, c_{m,s'}^{\dagger}\} = \delta_{n,m} \delta_{s,s'}$. The π -electron-ion interaction term is given by

$$H_{\pi\text{-ph}} = \alpha \sum_{n=1}^{N-1} \sum_{s=\pm 1} (u_{n+1} - u_n) (c_{n+1,s}^{\dagger} c_{n,s} + c_{n,s}^{\dagger} c_{n+1,s}), \quad (3)$$

where u_n is the displacement of the n -th site in the x direction from the perfectly periodic position $x = na$, with a as the lattice constant. The operator $H_{\pi\text{-ph}}$ couples the electronic states to the molecular geometry and provides a first-order correction to the hopping integral with α as the coupling constant. Finally, the nuclear Hamiltonian is taken to be

$$H_{\text{ph}} = \sum_{n=1}^N \frac{p_n^2}{2M} + \frac{K}{2} \sum_{n=1}^{N-1} (u_{n+1} - u_n)^2, \quad (4)$$

where M is the mass of the CH group, p_n is the momentum conjugate to u_n and K is an effective spring constant.

The SSH model is an effective [24] empirical model for non-interacting quasiparticles in PA. The electron-vibrational coupling and the hopping integral can be viewed as parameters in which screening and other high-energy effects have already been taken into account. The effect of the residual interactions that cannot be

accounted for by a simple renormalization of the one-electron Hamiltonian are completely neglected.

Throughout this work, we use the standard SSH parameters for PA [24]: $\alpha = 4.1$ eV/Å, $K = 21$ eV/Å², $t_0 = 2.5$ eV, $M = 1349.14$ eV fs²/Å² and $a = 1.22$ Å. Results using this set of parameters agrees qualitatively well with experimentally determined properties.

B. Photoinduced dynamics

To simulate excitation of the chain by a femtosecond laser pulse, an interaction with an electric field in dipole approximation is added to the SSH Hamiltonian. The electric field is taken into account to all orders and the dynamics is followed in the mean-field (Ehrenfest) approximation. Our approach resembles that of Johansson *et al.* [29, 30] and Streitwolf [31], but we dynamically propagate an *ensemble* of quantum-classical trajectories rather than a single trajectory that starts from the optimal geometry. Single-trajectory approaches [21, 22, 23, 29, 30, 31, 32] offer valuable insights into the time scales involved in the vibronic dynamics, but are insufficient for our purposes because including the decoherence effects requires averaging over the nuclear degrees of freedom. Further, during this study we have observed that the vibronic dynamics of the SSH chain tends to exhibit deterministic chaos and, hence, individual trajectories become inaccurate for sufficiently long integration times. By contrast, results for an ensemble of trajectories are meaningful even for long integration times, provided the shadowing theorem [33, 34] holds.

In the presence of a radiation field, the total Hamiltonian of the system assumes the form

$$H_S(t) = H_{SSH} + H_E(t), \quad (5)$$

where $H_E(t)$ describes the interaction of the chain with an external electric field $E(t)$ in the dipole approximation and Coulomb gauge,

$$H_E(t) = -(\mu_e + \mu_i)E(t). \quad (6)$$

Here $\mu_e = -|e| \sum_{n,s} x_n c_{n,s}^\dagger c_{n,s}$ and $\mu_i = +|e| \sum_n x_n$ are the electronic and ionic dipole moments, $x_n = na + u_n$ is the monomer position operator, a the lattice parameter and $-|e|$ the unit electronic charge. The Coulomb gauge is consistent with our open chain boundaries. As a field we use the femtosecond $\omega + 2\omega$ Gaussian pulses detailed in Table I at a variety of frequencies noted in the text.

In the mean-field approximation the nuclei move classically on a mean-field potential energy surface with forces given by [25, 26, 27, 28]

$$\dot{p}_n = -\langle \Psi(t) | \frac{\partial H_S(t)}{\partial u_n} | \Psi(t) \rangle, \quad (7)$$

where $|\Psi(t)\rangle$ denote the antisymmetrized \mathcal{N} -electron wave function. The electrons are assumed to respond

TABLE I: Parameters and labels defining the femtosecond laser pulses used $E(t) = \exp(-(t-T_c)^2/T_W^2)(\epsilon_\omega \cos(\omega t + \phi_\omega) + \epsilon_{2\omega} \cos(2\omega t + \phi_{2\omega}))$. Here $I_{2\omega}$ is the intensity of the 2ω component at maximum field strength.

Label	T_c (fs)	T_W (fs)	$\epsilon_{2\omega}$ (V Å ⁻¹)	$\epsilon_\omega/\epsilon_{2\omega}$	$I_{2\omega}$ (W cm ⁻²)
f1	900	300	8.70×10^{-3}	2.82	1.0×10^9
f2	900	300	4.00×10^{-2}	2.82	2.1×10^{10}
f3	50	10	8.70×10^{-3}	2.82	1.0×10^9
f4	50	10	4.00×10^{-2}	2.82	2.1×10^{10}

instantaneously to the nuclear motion and, hence, $|\Psi(t)\rangle$ satisfies the time-dependent Schrodinger equation

$$i\hbar \frac{\partial}{\partial t} |\Psi(t)\rangle = H_{\text{elec}}(\mathbf{u}(t), t) |\Psi(t)\rangle, \quad (8)$$

where H_{elec} contains the electronic and the electron-nuclei interaction terms of the total Hamiltonian, and $\mathbf{u} = (u_1, u_2, \dots, u_N)$. Equations (7) and (8) define the Ehrenfest method. Feedback between the fast and slow degrees of freedom is incorporated in both directions in an average self-consistent way. Note that the mean-field approximation avoids the expansion of the electronic wave function in terms of adiabatic basis functions. Equations (7) and (8) can therefore be integrated directly, making the implementation of the method particularly simple.

The electronic part of the total system Hamiltonian [Eq. (5)] reads

$$H_{\text{elec}}(t) = \sum_{n=1, s}^{N-1} [-t_0 + \alpha(u_{n+1} - u_n)] (c_{n+1, s}^\dagger c_{n, s} + c_{n, s}^\dagger c_{n+1, s}) + |e| \sum_{n=1, s}^N x_n c_{n, s}^\dagger c_{n, s} E(t). \quad (9)$$

Since $H_{\text{elec}}(t)$ is a single particle operator, the electronic properties of the system are completely characterized by the electronic reduced density matrix, defined by

$$\rho_{n,m}(t) = \sum_s \langle \Psi(t) | c_{n,s}^\dagger c_{m,s} | \Psi(t) \rangle. \quad (10)$$

From Eq. (8) it follows that the dynamics of $\rho_{n,m}(t)$ is governed by

$$\begin{aligned} i\hbar \frac{d}{dt} \rho_{n,m}(t) &= \sum_s \langle \Psi(t) | [c_{n,s}^\dagger c_{m,s}, H_{\text{elec}}(t)] | \Psi(t) \rangle \\ &= \sum_{m'} (h_{m,m'}(t) \rho_{n,m'}(t) - h_{m',n}(t) \rho_{m',m}(t)), \end{aligned} \quad (11)$$

where $h_{n,m}(t) = \langle n, s | H_{\text{elec}}(t) | m, s \rangle$ are the single-particle matrix elements of $H_{\text{elec}}(t)$, and $|n, s\rangle = c_{n,s}^\dagger |0\rangle$ where $|0\rangle$ is the vacuum state. In order to integrate this equation it is useful to employ an orbital decomposition for $\rho_{n,m}(t)$, as described below.

Let $|\epsilon, s\rangle$ be the eigenorbitals of the system at preparation time, defined by the eigenvalue relation $H_{\text{elec}}(t = 0)|\epsilon, s\rangle = \epsilon|\epsilon, s\rangle$. Using this basis, the initial electronic reduced density matrix can be expressed as

$$\rho_{n,m}(0) = \sum_{\epsilon, \epsilon'=1}^N \sum_s \langle \epsilon, s | n, s \rangle \langle m, s | \epsilon', s \rangle \langle \Psi(0) | c_{\epsilon, s}^\dagger c_{\epsilon', s} | \Psi(0) \rangle, \quad (12)$$

where $c_{\epsilon, s}^\dagger$ creates a fermion with spin s in the orbital with energy ϵ (i.e. $|\epsilon, s\rangle = c_{\epsilon, s}^\dagger |0\rangle$), and $\langle \Psi(0) | c_{\epsilon, s}^\dagger c_{\epsilon', s} | \Psi(0) \rangle$ characterizes the initial electronic distribution among the single particle states. In writing Eq. (12) we have employed the basis transformation function $c_{n, s} = \sum_{\epsilon=1}^N \langle n, s | \epsilon, s \rangle c_{\epsilon, s}$, and its hermitian conjugate, which takes into account the fact that $\langle \epsilon, s | n, s' \rangle = \langle \epsilon, s | n, s \rangle \delta_{s, s'}$ for the Hamiltonian under consideration. Upon time evolution we assume that $\rho_{n,m}(t)$ maintains the form in Eq. (12). That is,

$$\rho_{n,m}(t) = \sum_{\epsilon, \epsilon'=1}^N \sum_s \langle \epsilon(t), s | n, s \rangle \langle m, s | \epsilon'(t), s \rangle \times \langle \Psi(0) | c_{\epsilon, s}^\dagger c_{\epsilon', s} | \Psi(0) \rangle. \quad (13)$$

The utility of this ansatz is that if the time-dependent orbitals $|\epsilon(t), s\rangle$ satisfy the single-particle Schrodinger equation

$$i\hbar \frac{d}{dt} |\epsilon(t), s\rangle = H_{\text{elec}}(t) |\epsilon(t), s\rangle, \quad (14)$$

with initial conditions $|\epsilon(t=0), s\rangle = |\epsilon, s\rangle$, the reduced density matrix automatically satisfies the correct equation of motion [Eq. (11)].

With the exception of the simulations presented in Sec. III B 3, the initial electronic state $|\Psi(0)\rangle$ is taken to be a single Slater determinant for which

$$\langle \Psi(0) | c_{\epsilon, s}^\dagger c_{\epsilon', s} | \Psi(0) \rangle = \delta_{\epsilon, \epsilon'} f(\epsilon, s), \quad (15)$$

where $f(\epsilon, s)$ is the initial distribution function that takes values 0 or 1 depending on the initial occupation of each level with energy ϵ and spin s . In this case, $\rho_{n,m}(t)$ assumes the simplified form

$$\rho_{n,m}(t) = \sum_{\epsilon=1}^N \sum_s \langle \epsilon(t), s | n, s \rangle \langle m, s | \epsilon(t), s \rangle f(\epsilon, s). \quad (16)$$

Henceforth we drop spin labels since orbitals with opposite spin satisfy the identical equation of motion.

Given Eqs. (7) and (10) and the total Hamiltonian of the system Eq. (5), the equations for the nuclear trajectories are given as

$$\begin{aligned} \dot{u}_n(t) &= \frac{p_n(t)}{M}; \\ \dot{p}_n(t) &= -K(2u_n(t) - u_{n+1}(t) - u_{n-1}(t)) \\ &\quad + 2\alpha \text{Re} \{ \rho_{n, n+1}(t) - \rho_{n, n-1}(t) \} \\ &\quad - |e|E(t)(\rho_{n, n}(t) - 1). \end{aligned} \quad (17)$$

The chain is taken to be clamped so that $u_1(t) = u_N(t) = 0$ and $p_1(t) = p_N(t) = 0$ for all time, and Eq. (17) is valid for $n = 2, \dots, N-1$. In turn, the orbitals that form $\rho_{nm}(t)$ satisfy Eq. (14), so that

$$\begin{aligned} i\hbar \frac{d}{dt} \langle n | \epsilon(t) \rangle &= [-t_0 + \alpha(u_{n+1}(t) - u_n(t))] \langle n+1 | \epsilon(t) \rangle \\ &\quad + [-t_0 + \alpha(u_n(t) - u_{n-1}(t))] \langle n-1 | \epsilon(t) \rangle \\ &\quad + |e|E(t)(na + u_n(t)) \langle n | \epsilon(t) \rangle, \end{aligned} \quad (18)$$

for $n, \epsilon = 1, \dots, N$. Since the electrons are confined within the chain, $\langle n | \epsilon(t) \rangle = 0$ for $n \notin \{1, \dots, N\}$. Equations (17) and (18) constitute a closed set of $N(N+2)$ coupled first-order differential equations, which are integrated using the eighth-order Runge-Kutta method with step-size control [35].

C. The initial conditions

A crucial aspect of the problem is the choice of initial conditions. The oligomer is assumed to be in the ground electron-vibrational state. Hence, we first determine the optimal geometry of an N -membered oligomer with open boundaries and clamped ends ($u_1 = u_N = 0$) by an iterative self-consistent procedure, and then perform a normal mode analysis in the ground electronic surface as detailed in Ref. 36. This procedure provides the nuclear ground-state wave function in the harmonic approximation. A phase-space like description of the resulting nuclear quantum state is obtained by constructing the associated nuclear Wigner phase-space distribution [37, 38] function $\rho_{\text{W}}(\mathbf{u}, \mathbf{p})$, which is just the product of the Wigner distributions associated with each vibrational mode

$$\rho_{\text{W}}(\mathbf{u}, \mathbf{p}) = \prod_{j=1}^{N-2} \rho_j(Q_j(\mathbf{u}), P_j(\mathbf{p})). \quad (19)$$

Here $Q_j(\mathbf{u})$ is the normal mode coordinate of the j -th mode and $P_j(\mathbf{p})$ its conjugate momentum. In the ground state, the Wigner distribution of each normal mode is given by [37]

$$\rho_j(Q_j, P_j) = \frac{1}{\pi\hbar} \exp(-M\omega_j Q_j^2/\hbar) \exp(-P_j^2/\hbar\omega_j M), \quad (20)$$

where ω_j is the frequency of the j th mode. The $2N-4$ dimensional phase-space distribution in Eq. (19) completely characterizes the initial quantum state of the nuclei.

The ensemble of lattice initial conditions, $\{\mathbf{u}^i(0), \mathbf{p}^i(0)\}$, for the quantum-classical dynamics is obtained from a Monte Carlo sampling of the nuclear Wigner phase space distribution of Eq. (19). The average classical energy of the resulting ensemble coincides numerically with the zero-point energy of the lattice. The associated initial values for the orbitals $\{\langle n | \epsilon^i(0) \rangle\}$

are obtained by diagonalizing the electronic part of the Hamiltonian in the initial lattice geometries $\{\mathbf{u}^i(0)\}$. Each initial condition i , together with the equations of motion (17) and (18), defines a quantum-classical trajectory $(\mathbf{u}^i(0), \mathbf{p}^i(0), |\Psi^i(0)\rangle) \rightarrow (\mathbf{u}^i(t), \mathbf{p}^i(t), |\Psi^i(t)\rangle)$. The set is propagated using a parallel algorithm and used to obtain ensemble averages. In this manner, the dynamics reflects the effects of lattice fluctuations and the initial quantum phase-space distribution of the nuclei.

Since laser-induced symmetry breaking is an effect that depends on the third-order response of the system to the field, adequate convergence of the results with the number of initial conditions requires a large number of initial configurations, $\mathcal{O}(10^3 \times (2N - 4))$. This is the main computational bottleneck of the present approach and limits our analysis to modestly sized oligomer chains.

D. Dynamical observables

During the vibronic dynamics induced by the laser field the molecular geometry distorts and this, in turn, induces strong changes in the electronic wave function. Below we describe the geometric and spectroscopic observables that we use to follow the evolution of both nuclei and electrons.

Geometrical changes in the polymer backbone are characterized by the bond length alternation parameter r_n , which quantifies the homogeneity in the distribution of π electrons over the bonds. The ensemble average of this quantity is defined by

$$\begin{aligned} \langle r_n \rangle &= \frac{1}{\mathcal{M}} \sum_{i=1}^{\mathcal{M}} \frac{(-1)^n}{2} (l_{n-1}^i - l_n^i) \\ &= \frac{1}{\mathcal{M}} \sum_{i=1}^{\mathcal{M}} \frac{(-1)^n}{2} (2u_n^i - u_{n-1}^i - u_{n+1}^i), \end{aligned} \quad (21)$$

where l_n^i is the bond length between the n -th and $(n+1)$ -th atoms along the chain in the i -th member of the ensemble and \mathcal{M} is the cardinality of the ensemble. When the alternation between single and double bonds is perfect, the bond length alternation is constant (apart from end effects) and takes a value of $r_0 \approx 0.08 \text{ \AA}$. An enhancement in the electronic delocalization tends to equalize the bond lengths in the polymer resulting in $|r_n|/r_0 \ll 1$.

The state of the electronic degrees of freedom is completely characterized by the ensemble-averaged electronic reduced density matrix,

$$\bar{\rho}_{n,m}(t) = \frac{1}{\mathcal{M}} \sum_{i=1}^{\mathcal{M}} \rho_{n,m}^i(t) \quad (22)$$

where $\rho_{n,m}^i$ is defined by Eq. (10). The diagonal elements of $\bar{\rho}_{n,m}(t)$ represent the density of charge along the chain. The off-diagonal elements represent the electronic coherences between different sites.

A compact description of the electronic dynamics is offered by the polarization of the chain, defined by

$$\langle \mu(t) \rangle = \frac{|e|}{\mathcal{M}} \sum_{i=1}^{\mathcal{M}} \sum_{n=1}^N x_n^i(t) (1 - \rho_{n,n}^i), \quad (23)$$

where $x_n^i(t) = (na + u_n^i(t))$ is the position of site n at time t in the i -th trajectory. The first term in Eq. (23) comes from the dipole due to the nuclei, while the second one quantifies the electronic contributions. Any laser-induced symmetry breaking must manifest as a DC component in $\langle \mu(t) \rangle$. In order to isolate the zero-frequency component from the oscillatory terms we integrate the signal over time

$$\langle C(t) \rangle = \frac{1}{LT_W} \int_0^t dt' \langle \mu(t') \rangle. \quad (24)$$

This gives the net cumulative dipole induced by the field, weighted over the chain length L and the temporal pulse width T_W .

For each member of the ensemble the instantaneous eigenorbitals of the electronic Hamiltonian (including the field) are defined by the eigenvalue relation

$$H_{\text{elec}}^i(t) |\gamma^i(t)\rangle = \epsilon_\gamma^i(t) |\gamma^i(t)\rangle, \quad (25)$$

where $H_{\text{elec}}^i(t)$ is the electronic Hamiltonian for trajectory i at time t . At each instant in time the instantaneous eigenorbitals for different trajectories differ since each trajectory experiences a different vibronic evolution. For each trajectory, at a given t , the orbitals $|\epsilon^i(t)\rangle$ satisfying Eq. (18) may be expanded as a linear combination of the instantaneous eigenfunctions $|\gamma^i(t)\rangle$, $|\epsilon^i(t)\rangle = \sum_\gamma a_{\gamma,\epsilon}^i(t) |\gamma^i(t)\rangle$, where $a_{\gamma,\epsilon}^i(t) = \langle \gamma^i(t) | \epsilon^i(t) \rangle$. The occupation number n_γ^i of the instantaneous states is thus given by

$$n_\gamma^i(t) = \sum_{\epsilon,s} |\langle \gamma^i(t) | \epsilon^i(t) \rangle|^2 f(\epsilon, s) = \sum_{\epsilon,s} |a_{\gamma,\epsilon}^i|^2 f(\epsilon, s), \quad (26)$$

and varies as the system evolves. This contrasts with purely adiabatic dynamics with fixed level occupation. For the ensemble, we define the mean occupation and mean energy of the instantaneous eigenstates as

$$\langle \epsilon_\gamma(t) \rangle = \frac{1}{\mathcal{M}} \sum_{i=1}^{\mathcal{M}} \epsilon_\gamma^i(t), \quad \langle n_\gamma(t) \rangle = \frac{1}{\mathcal{M}} \sum_{i=1}^{\mathcal{M}} n_\gamma^i(t), \quad (27)$$

for $\gamma = 1, \dots, N$. These quantities are physically acceptable if the ordering of the eigenstates does not vary among trajectories, a property that we assume. Throughout the text the label γ is employed to number the instantaneous eigenstates of the oligomer in ascending order, with $\gamma = 1, N/2$ and $N/2 + 1$ denoting the lowest energy, HOMO and LUMO orbitals respectively.

III. RESULTS AND DISCUSSION

Consider the ability of $\omega+2\omega$ fields to induce symmetry breaking in PA. The dynamics is characterized using the observables discussed in Sec. IID as well as by the different contributions to the chain energy. Vibrational effects are made explicit by contrasting the vibronic dynamics of the oligomers with the evolution of a single trajectory for an equivalent but rigid system initially in the optimal geometry. The chain is made rigid by multiplying the mass of the CH groups by a factor of 10^6 . In this way the lattice is made to move a thousand times more slowly while maintaining the same value of the electron-ion interaction.

A. Initial state

We study neutral oligomers with 20 sites and 20 π electrons ($L \approx 23$ Å) initially in the ground electronic configuration. This size was selected because it reproduces qualitatively well the spectrum and dimerization pattern of longer chains without making the computational effort prohibitive. The initial state for the flexible chain consists of an ensemble of 100,000 initial conditions obtained by sampling the ground-state nuclear Wigner distribution (Sec. IIC).

The resulting electronic and geometrical properties of the chain are shown in Fig. 1. The initial geometry of the chain (Fig. 1C) consists of a perfect alternation of double and single bonds, yielding $\langle r_n \rangle \sim 0.08$ Å. The open ends boundary condition results in a stronger dimerization near the edges of the oligomer. The structure is centro-symmetric with the inversion center residing between sites 10 and 11. The single-particle spectrum (Fig. 1D and Table II) has a total width of $4t_0 = 10$ eV. It consists of $N/2$ fully occupied π (valence) states and $N/2$, initially empty, π^* (conduction) states, separated by an energy gap $2\Delta = 1.8$ eV. The reduced density matrix (Fig. 1A-B) is concentrated along the diagonal of the plot reflecting the bonding pattern of the oligomer, with the spatial electronic coherence (measured by the magnitude of the off-diagonal matrix elements) being $\sim 10 - 15$ units.

Note that the *average* geometrical and spectroscopic properties of the ensemble coincide with the ones obtained from a single configuration in the optimal geometry. However, within the ensemble there is a distribution of values for the properties, displaying important deviations from the average. For example, we find that the ensemble of orbital energies form bands of states distributed in a Gaussian fashion about the band averages. The banded-Gaussian distribution in energy space is a direct result of the Gaussian distribution of the initial geometries. The band-averages $\langle \epsilon_i \rangle$ and bandwidths σ_i are enumerated in Table II. Note that the bandwidth of the electronic levels near the energy gap ($i = 10 - 11$) is considerably broader than the one displayed by states

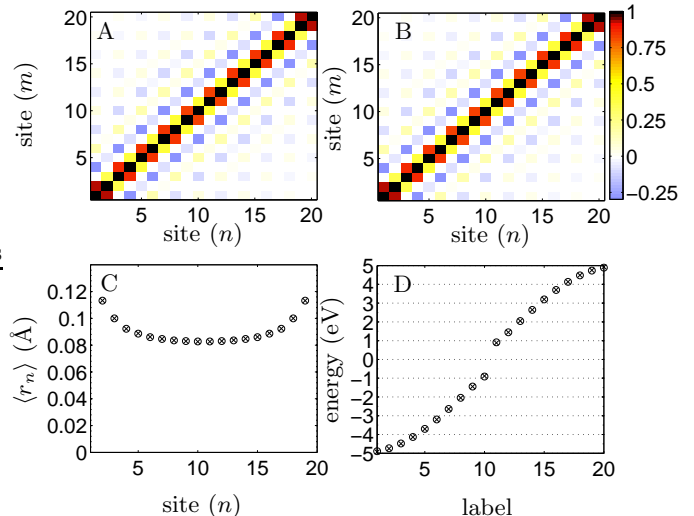


FIG. 1: Nuclear and electronic properties of a 20 atoms + 20 π electrons SSH-type chain in the ground-state configuration. Properties of the chain in the optimal geometry are compared with the average results obtained from an ensemble of 100,000 initial configurations. The upper panels show the reduced density matrix (chosen to be real) for (A) the optimal geometry and (B) the ensemble of initial states. The color bar is given in the far right. Panel (C): bond length alternation along the chain and (D) the single-particle spectrum. (o) - the optimal geometry; (x) - the ensemble average. In both cases, the initial average momentum for each atom is zero.

TABLE II: Initial single particle spectrum for the 20 site neutral PA oligomer. The energies ϵ_i^0 were obtained at the optimal geometry, while $\langle \epsilon_i \rangle$ denote the average orbital energies for the ensemble. The ensemble of orbital energies form energy bands distributed in a Gaussian manner about the band centers, $f(\epsilon_i) = \frac{1}{\sqrt{2\pi}\sigma_i} \exp(-(\epsilon - \langle \epsilon_i \rangle)^2 / 2\sigma_i^2)$, where σ_i is the standard deviation.

i	ϵ_i^0 (eV)	$\langle \epsilon_i \rangle$ (eV)	σ_i (eV)	i	ϵ_i^0 (eV)	$\langle \epsilon_i \rangle$ (eV)	σ_i (eV)
1	-4.893	-4.930	0.034	11	0.914	0.883	0.130
2	-4.735	-4.755	0.039	12	1.445	1.444	0.107
3	-4.479	-4.491	0.046	13	2.045	2.049	0.091
4	-4.131	-4.141	0.053	14	2.640	2.646	0.079
5	-3.701	-3.708	0.061	15	3.199	3.206	0.068
6	-3.199	-3.206	0.068	16	3.701	3.708	0.061
7	-2.640	-2.646	0.079	17	4.131	4.141	0.053
8	-2.045	-2.049	0.091	18	4.479	4.491	0.046
9	-1.445	-1.444	0.107	19	4.735	4.755	0.039
10	-0.914	-0.883	0.130	20	4.893	4.930	0.034

near the band edges.

Last, due to residual anharmonicities around the equilibrium geometry, the distribution in Eq. (19) is not completely stationary. Rather, the average values of the initial state display some fluctuations under free evolution. These fluctuations are very small, introducing only small changes to Fig. 1, of the order of 1% in the band-gap energy and of 3% in the bond length alternation.

B. Rigid vs. flexible chain dynamics

For rigid chains, changes in the electronic spectrum can only arise from the Stark shifts induced by the laser field. By contrast, for flexible chains there is a continuous exchange of energy between the electronic and nuclear degrees of freedom during the photoexcitation process. Below we present two illustrative examples of the photoinduced dynamics in PA. First we consider the case in which the lattice is photoexcited with a 10 fs pulse (Sec. III B 1). For such short pulses very little excited state dynamics occurs during the pulse. In the wake of the pulse we observe coherent vibrational breathing motion that decays in ~ 200 fs due to vibrational energy redistribution. We then consider excitation with a 300 fs pulse (Sec. III B 2). In this case the laser does not generate a breathing motion of the lattice. Rather, we observe a gradual increase in the electronic delocalization, accompanied by a concurrent change in the average spectroscopic and geometrical parameters of the chain.

Last, in Sec. III B 3 we quantify the time-scale for electronic dephasing for chains of different lengths.

1. The dynamics induced by a 10 fs pulse

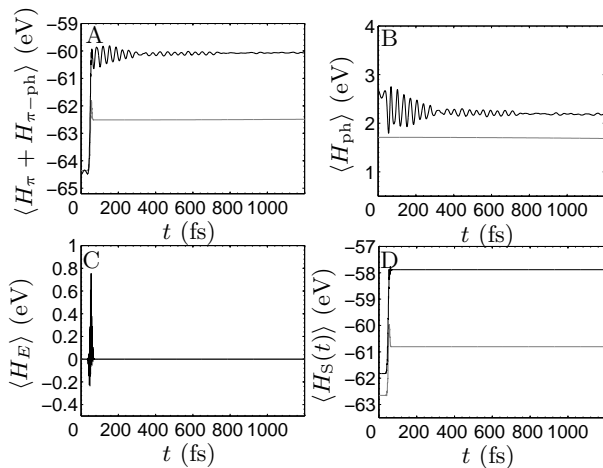


FIG. 2: Energy contributions during the dynamics of PA under the influence of pulse **f4** with $\hbar\omega = 1.3$ eV and $\phi_{2\omega} - 2\phi_\omega = 0$ for the rigid (gray lines) and flexible (black lines) chain. Panel (A): the electronic kinetic energy (including electron-ion interactions), (B): purely nuclear energy, and (C): radiation-matter interaction. The total energy is shown in (D).

The different contributions to the rigid and flexible chain energy during and after photoexcitation with a 10 fs $\omega + 2\omega$ pulse (laser field **f4** in Table I) with $\hbar\omega = 1.3$ eV are shown in Fig. 2. Initially, the flexible chain has 0.83 eV more energy than its rigid counterpart due to zero-point motion in the ground electronic state. Secondly, after photoexcitation, the rigid chain gains 1.85 eV from

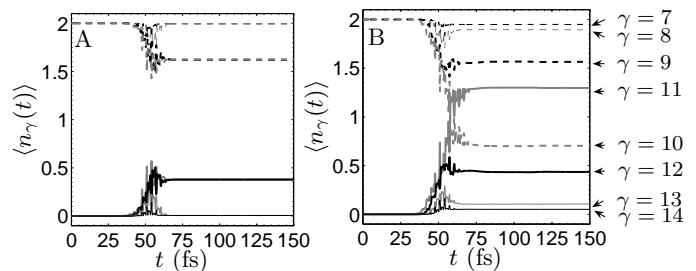


FIG. 3: Occupation numbers of the instantaneous eigenstates near the band gap for the (A) rigid and (B) flexible chain during the dynamics induced by pulse **f4** with $\hbar\omega = 1.3$ eV and $\phi_{2\omega} - 2\phi_\omega = 0$.

the laser while the average energy absorbed by the ensemble of flexible chains is 3.9 eV. This enhanced absorption of energy of the flexible chain is due to spectral broadening of states which form bands, with the broadening being especially large near the band gap (recall Table II). As exemplified in Fig. 3, this results in a wider set of electronic levels being populated during photoexcitation. In both cases, the occupation numbers and the single particle spectrum display the electron-hole symmetry of the SSH Hamiltonian.

Figure 4 shows the evolution of the bond length alternation parameter (upper panel) and the mean instantaneous orbital energies for states near the energy gap (lower panel) of the flexible chain. The photoexcitation of the chain initiates a complex highly nonlinear vibronic evolution. The lattice is set to vibrate and large scale oscillations in the bond length alternation are observed. By $t = 67$ fs the chain has reversed the sense of its dimerization and establishes a coherent “breathing” oscillation of the bond length alternation in which $\langle r_n(t) \rangle$ oscillates between the two senses of dimerization. Several carbon-carbon stretching vibrational modes with periods between 32 – 40 fs enter into the initial lattice dynamics. The breathing motion, however, is not long lived and the amplitude of the oscillations display an initial fast exponential decay with a characteristic time-scale of $\sim 90 - 130$ fs, followed by a slower damping. By $t \sim 400$ fs most of the vibrational modes initially excited have already decayed, and gradually the system approaches a state of internal equilibrium through internal vibrational energy redistribution.

These changes in the lattice geometry are reflected as changes in the single-particle spectrum. Upon initial photoexcitation the two states near the energy gap come very close to each other in less than 20 fs and the band-gap energy fluctuates following the breathing oscillation of the bond-length alternation. A dip (crest) in the bond-length alternation corresponds to a minimum (maximum) in the gap energy. Concurrent with the dimerization pattern, the energy gap exhibits strong initial oscillations at time scales between 30-40 fs that rapidly decay, followed by a slower damping. The band-gap energy eventually reaches

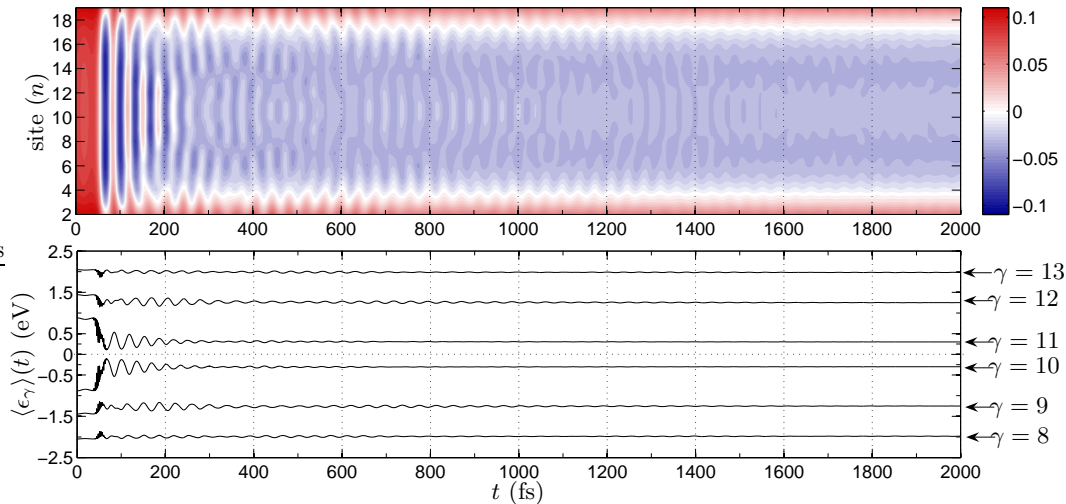


FIG. 4: Vibronic dynamics of PA induced by pulse **f4** with $\hbar\omega = 1.3$ eV and $\phi_{2\omega} - 2\phi_\omega = 0$. The upper panel shows contours of the bond length alternation parameter [defined in Eq. (21)]. The lower panel, the mean instantaneous energies for the single-particle states near the energy gap.

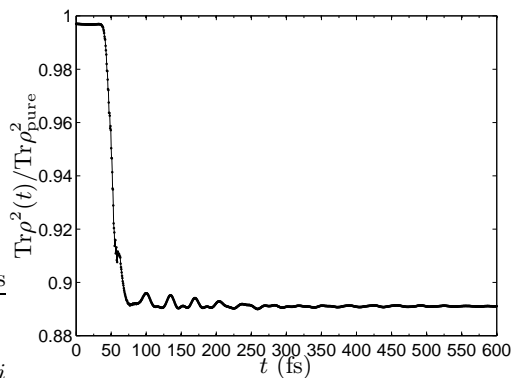


FIG. 5: Decoherence during the dynamics of the flexible chain induced by pulse **f4** (10 fs wide, centered at 50 fs) with $\hbar\omega = 1.3$ eV and $\phi_{2\omega} - 2\phi_\omega = 0$.

an equilibrium value of ~ 0.6 eV. The remaining energy levels also oscillate on time-scales determined by the different vibrational modes of the chain. We observe that states around the band-gap couple to vibrational modes whose period is ~ 38 fs, while states near the band edges couple to lower frequencies modes.

An estimate of the electronic decoherence that occurs during and after the pulse is provided by measuring the purity [39] $\text{Tr}\rho^2 = \sum_{n,m} \bar{\rho}_{n,m} \bar{\rho}_{m,n}$, where $\bar{\rho}_{n,m}$ are the matrix elements of the ensemble-averaged electronic reduced density matrix [Eq. (22)]. For pure systems with a $\rho_{n,m}(t)$ of the form in Eq. (16), as is the case of the rigid chain, $\text{Tr}\rho_{\text{pure}}^2$ is a constant equal to $2\mathcal{N}$ where \mathcal{N} is the number of electrons. For mixed states $\text{Tr}\rho_{\text{mixed}}^2 \leq \text{Tr}\rho_{\text{pure}}^2$ and its decay offers insight into the decoherence time scales introduced by the coupling to the

vibrational modes. Figure 5 shows the evolution of $\text{Tr}\rho^2$ for the flexible chain. The system begins in a state that is almost pure with $\text{Tr}\rho^2/\text{Tr}\rho_{\text{pure}}^2 = 0.997$. Upon photoexcitation the purity displays a sharp drop at ~ 40 fs, followed by some modulation in time scales commensurate with the vibrational periodicities of the chain. These modulations decay rapidly and the purity stabilizes at 0.89 after ~ 400 fs.

The dynamical behavior exemplified by our simulations describes quite well the main trends observed in recent sub-10 fs experiments that have been performed on PA [40] and PPV [41] samples: initial fast decay of the breathing motion (order of 200 fs) followed by a slower damping. Previous studies of the excited state dynamics in PA did not capture the decay since they only consider the evolution of a single trajectory. However, the time scales that we observe for the energy gap fluctuations (32-38 fs) are somewhat larger than the ones reported for PA of 31 fs and 23 fs. This is a consequence of the parameters employed for the Hamiltonian.

We have observed that the basic features of the vibronic dynamics described above also apply to longer oligomers. However, in the long chain limit the two states near the energy gap can become degenerate, forming soliton-antisoliton pairs [24], unlike to the case described above.

2. The dynamics induced by a 300 fs pulse

Consider now dynamics under the longer (300 fs) pulse **f1** with $\hbar\omega = 1.18$ eV. Here the pulse time width is long compared with the typical optical-phonon vibrational modes. Figure 6 and 7 show the different energy contributions to the chain during the dynamics and the

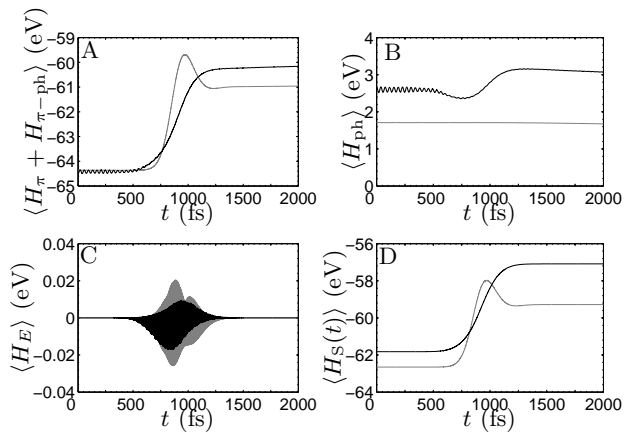


FIG. 6: Energy contributions during the dynamics of PA under the influence of pulse **f1** with $\hbar\omega = 1.18$ eV and $\phi_{2\omega} - 2\phi_\omega = 0$. Panel (A) electronic kinetic energy (including electron-ion interactions), (B) the purely nuclear energy, and (C) the radiation-matter interaction. The total energy is shown in (D). The gray and black lines correspond to the rigid and flexible chains, respectively.

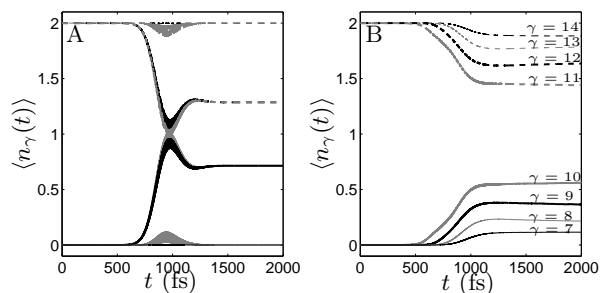


FIG. 7: Occupation numbers of the instantaneous eigenstates near the energy gap during the dynamics induced by pulse **f1** with $\hbar\omega = 1.3$ eV and $\phi_{2\omega} - 2\phi_\omega = 0$. (A) The rigid chain; (B) flexible case.

instantaneous occupation numbers for states near the energy gap, respectively. As before, due to broad nature of its transition frequencies the flexible chain absorbs 1.36 eV more energy from the field, with a wider range of electronic levels being populated during the process. The large-scale oscillations observed previously in the average electronic and nuclear energy for the flexible chain (Fig. 2A-B) are no longer present.

The origin of this difference in behavior is readily identified by considering the bond length alternation and the single particle spectrum during the dynamics (Figure 8). During the first 400 fs the bond-length alternation and the transition frequencies display minor oscillations. These oscillations arise because our initial state is not an exact eigenstate of the Hamiltonian due to ground state residual lattice anharmonicities. Upon photoexcitation the bond lengths in the chain slowly equalize in order to improve electronic delocalization along the chain that permits accommodating the electrons that

have been photoexcited. After the pulse the bond length alternation settles at $\sim 0.03\text{\AA}$. These changes in the lattice geometry are accompanied by a 0.7 eV red shift of the energy gap. However, contrary to the dynamics under the 10 fs pulse, the lattice does not establish a breathing motion. Instead the mean geometrical observables and spectroscopic quantities display a slow and steady change from the perfectly dimerized lattice to a chain with increased electronic delocalization. In essence, the frequency width of the pulse is not broad enough to bring about a coherent breathing motion of the chain. The latter requires participation of many vibrational states. These features of the vibronic dynamics induced by 300 fs pulses also persist when considering longer oligomers.

Decoherence occurs slowly and steadily during the time that the system is being driven by the laser field (Fig. 9). No modulations of $\text{Tr}\rho^2$ or further decoherence are observed after the pulse, and $\text{Tr}\rho^2/\text{Tr}\rho_{\text{pure}}^2$ stabilizes at ~ 0.88 . Computations discussed below show that the electronic dephasing time is of the order of 2.5 fs. Hence, the limiting step in the decoherence process is not the rate at which lattice-induced decoherence occurs, but the rate at which the field is able to establish new superposition states that then rapidly decohere.

3. How fast is the electronic dephasing?

A measure of the timescale for the electronic dephasing induced by intramolecular vibrational motions can be obtained by following the field-free evolution of neutral chains initially in an electronic superposition state. In a full quantum mechanical analysis, nuclear evolution on alternative electronic potential energy surfaces leads, in general, to electronic coherence loss. In our quantum-classical picture the electronic dephasing is captured by the distribution and evolution of orbital energies contained within the initial ensemble (recall Table II).

A detailed calculation reveals the features of this dephasing. Figure 10 shows the time-dependence of the polarization for PA oligomers initially prepared in a superposition $|\Psi(0)\rangle = \frac{1}{\sqrt{2}}(|G\rangle + |E\rangle)$, where $|G\rangle$ and $|E\rangle$ are the N -particle ground and first-excited electronic states. The initial nuclear distribution is taken to be the one obtained in the ground electronic surface, and $|E\rangle = c_{e''+1,s'}^\dagger c_{e'',s'}|G\rangle$ is generated by instantaneously promoting an electron from the HOMO to the LUMO orbital of the chain, so that $e'' = N/2$. For chains with 4 sites the polarization displays a fast initial decay, and observes recurrences every ~ 30 fs. In a full quantum mechanical analysis these recurrences arise from the time dependence of the overlap of the nuclear wavefunctions in the ground and excited electronic states. In this quantum-classical picture, the recurrences are captured by the time-dependence of the orbital energies during the dynamics. Note that between consecutive recurrences the amplitude of the polarization gets reduced and $\langle\mu(t)\rangle$ dies in hundreds of femtoseconds. For longer chains these re-

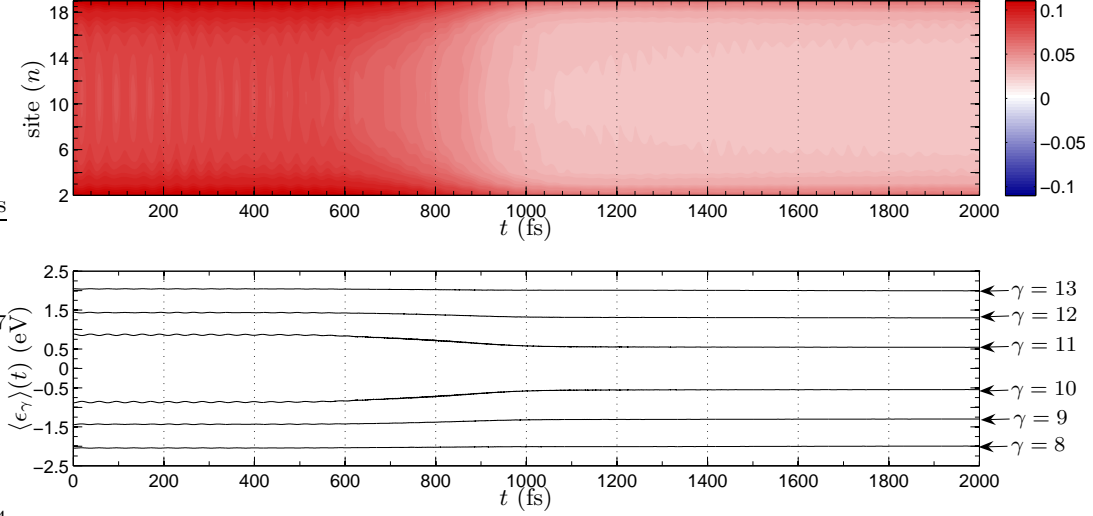


FIG. 8: The vibronic dynamics of PA induced by pulse **f1** with $\hbar\omega = 1.18$ eV and $\phi_{2\omega} - 2\phi_\omega = 0$. The upper panel shows contours of the bond length alternation parameter (defined in Eq. (21)). The lower panel shows the mean instantaneous energies for the single-particle states near the energy gap.

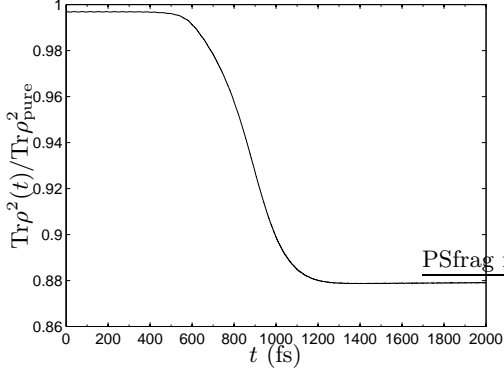


FIG. 9: Decoherence during the dynamics of the flexible chain induced by pulse **f1** (300 fs wide, centered at 900 fs) with $\hbar\omega = 1.18$ eV and $\phi_{2\omega} - 2\phi_\omega = 0$.

currences are less important and the dephasing time is basically determined by the initial decay of the polarization which occurs in less than 10 fs, with a characteristic timescale of 2.5 fs. These time-scales are in agreement with electronic dephasing timescales that have been determined in other systems using a fully quantum treatment [42].

C. Laser-induced symmetry breaking

In the previous sections we identified important ways in which the vibronic couplings influence the photoinduced dynamics of π -conjugated systems. The coupling introduces: (i) broadening of the electronic transitions

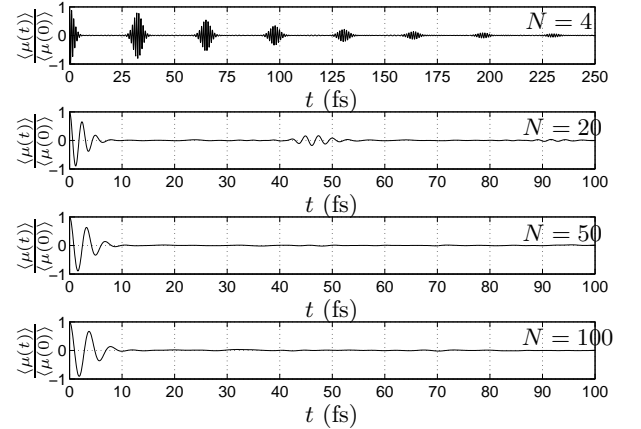


FIG. 10: Time dependence of the polarization $\langle \mu(t) \rangle$ for neutral flexible PA chains with N sites. The initial state is a superposition, with equal coefficients, between the ground and first excited electronic state. The nuclei are taken to be initially in the ground-state configuration.

(see Table II, and Figs. 3 and 7), (ii) pronounced changes in the mean single-particle spectrum (see Figs. 4 and 8), (iii) internal relaxation mechanisms, and (iv) ultrafast dephasing (see Figs. 5, 9 and 10). Because of this, when using lasers to control a dynamical process in this class of systems, the laser frequencies may become detuned from the desired transition and the control may be diminished by broadening of the electronic levels and internal relaxations. Here we investigate the extent to which these additional complexities affect the ability to induce symmetry breaking using the ω vs. 2ω coherent control sce-

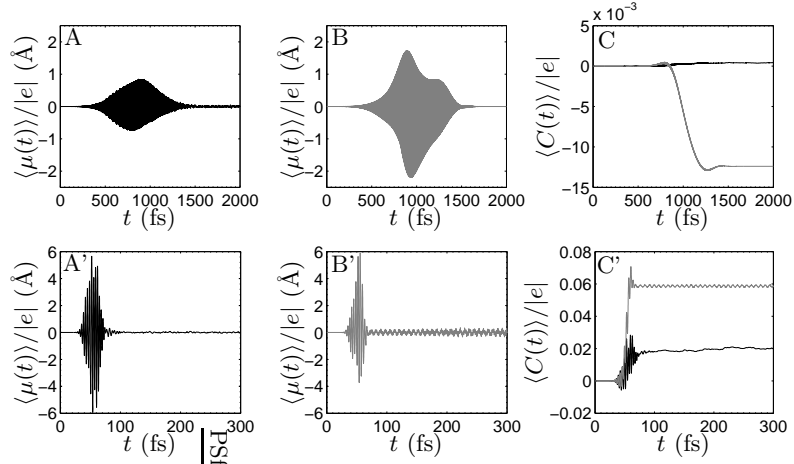


FIG. 11: First moment of the charge distribution during and after photoexcitation with a symmetry breaking $\omega + 2\omega$ laser field. (A) the flexible and (B) the rigid chain under the influence of pulse **f1** with $\hbar\omega = 1.18$ eV and $\phi_{2\omega} - 2\phi_\omega = 0$. Panel (C) the resultant cumulative dipoles $\langle C(t) \rangle$ (black line, flexible chain; gray line, rigid case). Parts (A')-(C') as in (A)-(C) but for the **f4** pulse with $\hbar\omega = 1.3$ eV and $\phi_{2\omega} - 2\phi_\omega = 0$.

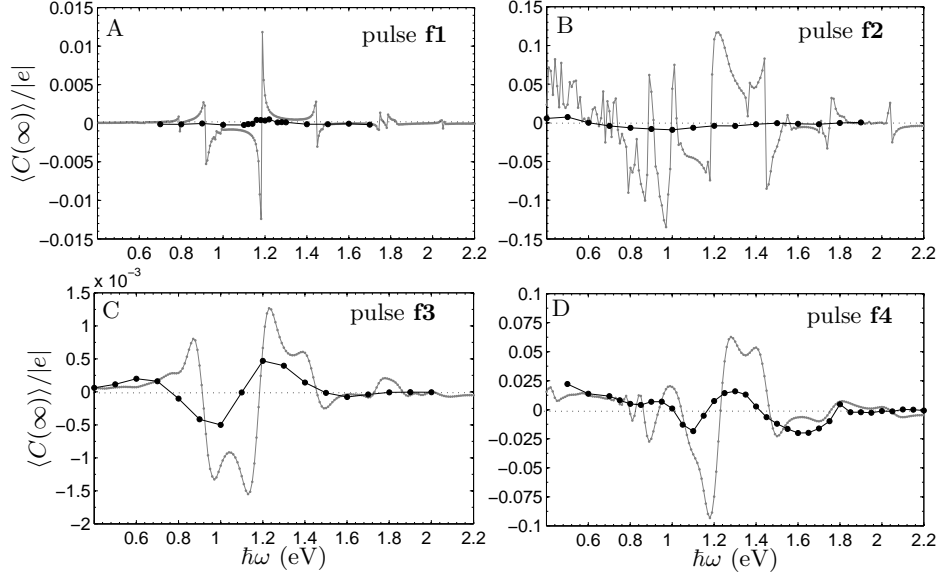


FIG. 12: Frequency dependence of the degree of symmetry breaking generated by an $\omega + 2\omega$ field in rigid (gray) and flexible (black) PA oligomers with 20 sites. The initial energy gap of the oligomer is $2\Delta = 1.8$ eV. The plots show the asymptotic cumulative dipole $\langle C(\infty) \rangle$ after photoexcitation with pulses (A) **f1**, (B) **f2**, (C) **f3** and (D) **f4**, using $\phi_{2\omega} - 2\phi_\omega = 0$.

nario.

The results presented in this section focus on effects that depend on the relative phase of the laser field. This is because symmetry breaking contributions that depend on the carrier envelope phase are typically difficult to control (although not impossible, see e.g., Ref. 43) since it requires an experimental arrangement that permits locking the carrier envelope phase of the incident radiation and that controls the position of the center of mass of the molecule with respect to the laboratory reference frame. This contrasts with relative-phase control that is unaffected by the center of mass motion and only requires

manipulating the relative phase between the two central frequency components of the $\omega + 2\omega$ field.

We consider the evolution of rigid and flexible chains under the influence of the laser pulses in Table I, for different laser frequencies. The parameters chosen for the laser pulses encompass four illustrative cases: dynamics induced by weak and moderately strong pulses with time envelopes that are either short or long with respect to the typical 30-40 fs optical-phonon vibrational period. Specifically, pulses **f1** and **f2** induce weak and strong-field dynamics, respectively, when the time-width of the pulse is relatively long (300 fs). By contrast, pulses **f3**

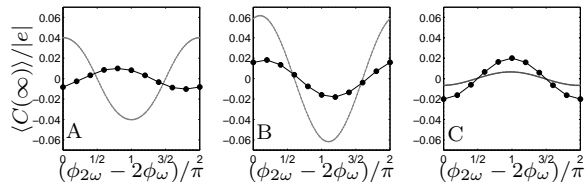


FIG. 13: The degree of symmetry breaking induced by an $\omega + 2\omega$ field in rigid (gray) and flexible (points) PA, as a function of the relative phase $\phi_{2\omega} - 2\phi_\omega$ of the laser. The figures show the mean cumulative dipole $\langle C(\infty) \rangle$ after photoexcitation with: (A) pulse **f2** with $\hbar\omega = 0.9$ eV; (B) pulse **f4** with $\hbar\omega = 1.3$ eV; and (C) pulse **f4** with $\hbar\omega = 1.6$ eV.

and **f4** offer insight into the weak- and strong-field control when the laser pulses are short (10 fs), and of the order of the electronic dephasing time, permitting only a limited degree of excited state dynamics during the pulse.

Consider first the dynamics in the weak-field/long-pulse (**f1**) and strong-field/short-pulse (**f4**) regimes. The relevant observable here is the polarization of the chain $\langle \mu(t) \rangle$ [Eq. (23)] which quantifies the symmetry breaking. Figure 11 shows representative results. Initially $\langle \mu \rangle = 0$, reflecting the symmetric distribution of electrons over the chain. As soon as the laser is turned on, dipoles are induced in the system, oscillating with the frequencies of the field and various harmonics. The harmonic of interest is the zero-frequency (DC) component, appearing at the 3rd, 5th, etc. order response to the $\omega + 2\omega$ field. These harmonics can be extracted by integrating the signal over time [see Eq. (24)], yielding the cumulative dipoles $\langle C(t) \rangle$ shown in Fig. 11C and Fig. 11C'. We denote the mean asymptotic value of $\langle C(t) \rangle$ after the pulse as $\langle C(\infty) \rangle$. As can be seen, all symmetry breaking effects induced by the $\omega + 2\omega$ field are achieved while the system is being driven by the laser field. Once the field is turned off, the zero-frequency component disappears so that $\langle C(t) \rangle$ becomes constant and net dipoles no longer persist. This is because systems with discrete, non-degenerate, spectra cannot sustain net dipoles after the pulse.

In the rigid case the zero-frequency term constitutes an important component of $\langle \mu(t) \rangle$ and both **f1** and **f4** pulses generate a net dipole while the pulse is on. By contrast, when pulse **f1** is applied on the flexible chain (Fig. 11 upper panels) the electron-vibrational couplings mute most of the effect. However, by applying a shorter pulse (lower panels) it is possible to generate net dipoles that are of the same order of magnitude as the ones observed for the rigid chain. In essence, by using shorter pulses one is limiting the detrimental effects that the excited state vibronic couplings exert on the control.

A complementary perspective on the influence of the vibronic couplings on the photoinduced control is obtained by considering the dependence of the symmetry breaking effect on the laser frequency ω . Figure 12 shows the asymptotic cumulative dipoles $\langle C(\infty) \rangle$ observed in

flexible and rigid chains after photoexcitation with pulses **f1-f4** for different laser frequencies. In the rigid case, the ω vs. 2ω coherent control scenario is very robust, inducing net dipoles at most driving frequencies and with pulses of any time-width and intensity. The effect shows sharp resonances at selected frequencies. The origin of these resonances can be identified by comparing the control map to the single particle spectrum of the rigid chain (Table II). Consider, for instance, the resonances displayed in Fig. 12A at $\hbar\omega = 0.9, 1.18$ and 1.42 eV. At these frequencies the quantity 2ω coincides with the HOMO \rightarrow LUMO, HOMO \rightarrow LUMO+1 (or HOMO-1 \rightarrow LUMO), and HOMO-1 \rightarrow LUMO+1 transition frequencies, respectively. By applying stronger pulses (e.g. Fig. 12B) it is possible to exploit high order multiphoton processes to generate dc terms, resulting in a complicated frequency dependence of the degree of control.

The control map in the flexible chain is remarkably different. In flexible chains, in order to generate appreciable symmetry breaking it is necessary to work with either sufficiently short pulses, so that only limited excited state dynamics occurs during the pulse (Figs. 12C-D), or to apply stronger fields, as in Fig. 12B, in which the evolution imposed by the field becomes dominant. When using short pulses, the resonance structure previously observed in the rigid-chain control case is partially maintained. However, in the case of long pulses the fine features observed in the rigid chain are washed away by the broadening of the electronic transitions, with only the rough features in the control map being maintained. Interestingly, when applying short pulses at selected frequencies it is possible to obtain a higher degree of symmetry breaking in the flexible chain than in the rigid chain. However, the maximum control attainable (as a function of ω) is always attenuated by the electron-vibrational couplings.

Importantly, in all cases the sign and magnitude of symmetry breaking can be manipulated by varying the relative phase between the two components of the field. Figure 13 exemplifies this dependence for selected frequencies and pulses. The electron-vibrational couplings in the system do not destroy the phase control of the electronic dynamics, but merely attenuate its magnitude. It follows then that it is possible to use the techniques of coherent control to manipulate electronic dynamics even in the presence of significant vibronic couplings. The attenuation of the effect can be overcome by using stronger pulses or by working with laser pulses that are short or comparable with the time-scale for electronic dephasing. Similar results were found in sample studies on longer chains.

IV. CONCLUSIONS

We have investigated the possibility of inducing electronic transport in conjugated polymers by irradiating the sample with $\omega + 2\omega$ lasers. To do so, we have followed the highly nonlinear dynamics of the electronic

and vibrational degrees of freedom in *trans*-polyacetylene oligomers in the presence of $\omega+2\omega$ laser pulses of different durations and intensities, and for a variety of frequencies. The simulations are performed in the mean field approximation, in which the nuclei are treated classically and the electrons quantum mechanically. The dynamics is followed for an ensemble of lattice initial conditions obtained by sampling the ground-state nuclear Wigner distribution function in the harmonic approximation.

Several important ways in which the electron-vibrational couplings in π -conjugated systems modify the photoinduced dynamics have been identified. The vibronic couplings introduce broadening of the electronic transitions and can cause ultrafast dephasing in the electronic dynamics, as well as pronounced changes in the mean single-particle spectrum and IVR.

The simulations reveal that the vibronic couplings can have strong detrimental effects on the control. In fact,

it is difficult to induce and control electronic transport when the laser pulses are longer than the typical carbon-carbon vibrational period of ~ 30 fs, unless the pulse intensities are strong enough to completely dominate the dynamics. However, even in the presence of significant vibronic couplings, limited laser control of the electronic dynamics is possible via the use of pulses whose durations are comparable to the electronic dephasing timescale (~ 10 fs).

These results provide insight into the way coherent control works in large molecular systems with significant electron-vibrational couplings, and offer a characterization of the time-scale of decay of photoinduced breathers in conjugated polymers. We expect that the set of phenomena investigated here will be of generic importance in a wide range of materials characterized by significant electron-vibrational couplings.

-
- [1] A. J. Heeger, *Rev. Mod. Phys.* **73**, 681 (2001).
- [2] R. H. Friend, R. W. Gymer, A. B. Holmes, J. H. Burroughes, R. N. Marks, C. Taliani, D. D. C. Bradley, D. A. dos Santos, J. L. Brédas, M. Logdlund, et al., *Nature* **397**, 121 (1999).
- [3] S. R. Forrest, *Nature* **428**, 911 (2002).
- [4] M. Shapiro and P. Brumer, *Principles of the Quantum Control of Molecular Processes* (John Wiley & Sons, New York, 2003).
- [5] I. Franco and P. Brumer, *J. Phys. B* **41**, 074003 (2008).
- [6] I. Franco and P. Brumer, *Phys. Rev. Lett.* **97**, 040402 (2006).
- [7] Y. Y. Yin, C. Chen, D. S. Elliott, and A. V. Smith, *Phys. Rev. Lett.* **69**, 2353 (1992).
- [8] E. Dupont, P. B. Corkum, H. C. Liu, M. Buchanan, and Z. R. Wasilewski, *Phys. Rev. Lett.* **74**, 3596 (1995).
- [9] A. Haché, Y. Kostoulas, R. Atanasov, J. L. P. Hughes, J. E. Sipe, and H. M. van Driel, *Phys. Rev. Lett.* **78**, 306 (1997).
- [10] J. Güdde, M. Rohleder, T. Meier, S. W. Koch, and U. Höfer, *Science* **318**, 1287 (2007).
- [11] M. Schiavoni, L. Sanchez-Palencia, F. Renzoni, and G. Grynberg, *Phys. Rev. Lett.* **90**, 094101 (2003).
- [12] G. Kurizki, M. Shapiro, and P. Brumer, *Phys. Rev. B* **39**, 3435 (1989).
- [13] R. Atanasov, A. Haché, J. L. P. Hughes, H. M. van Driel, and J. E. Sipe, *Phys. Rev. Lett.* **76**, 1703 (1996).
- [14] K. A. Pronin and A. D. Bandrauk, *Phys. Rev. B* **69**, 195308 (2004).
- [15] E. J. Mele, P. Král, and D. Tománek, *Phys. Rev. B* **61**, 7669 (2000).
- [16] I. Franco, M. Shapiro, and P. Brumer, *Phys. Rev. Lett.* **99**, 126802 (2007).
- [17] J. Lehmann, S. Kohler, and P. Hänggi, *J. Chem. Phys.* **118**, 3283 (2003).
- [18] J. Lehmann, S. Kohler, V. May, and P. Hänggi, *J. Chem. Phys.* **121**, 2278 (2004).
- [19] H. P. Breuer and F. Petruccione, *The Theory of Open Quantum Systems* (Oxford University Press, New York, 2002).
- [20] U. Weiss, *Quantum Dissipative Systems* (World Scientific, Singapore, 1999), 2nd ed.
- [21] S. Tretiak, A. Saxena, R. L. Martin, and A. R. Bishop, *Phys. Rev. Lett.* **89**, 097402 (2002).
- [22] S. Tretiak, A. Saxena, R. L. Martin, and A. R. Bishop, *Proc. Natl. Acad. Sci. USA* **100**, 2185 (2003).
- [23] I. Franco and S. Tretiak, *J. Am. Chem. Soc.* **126**, 12130 (2004).
- [24] A. J. Heeger, S. Kivelson, J. R. Schrieffer, and W. P. Su, *Rev. Mod. Phys.* **60**, 781 (1988).
- [25] J. C. Tully, in *Classical and Quantum Dynamics in Condensed Phase Simulations*, edited by B. Berne, G. Ciccotti, and D. F. Coker (World Scientific, Singapore, 1998), pp. 700–720.
- [26] L. L. Halcomb and D. J. Diestler, *J. Chem. Phys.* **84**, 3130 (1986).
- [27] F. A. Bornemann, P. Nettesheim, and C. Schütte, *J. Chem. Phys.* **105**, 1074 (1996).
- [28] O. V. Prezhdo and V. V. Kisil, *Phys. Rev. A* **56**, 162 (1997).
- [29] A. Johansson and S. Stafström, *Phys. Rev. B* **65**, 045207 (2002).
- [30] A. Johansson and S. Stafström, *Phys. Rev. Lett.* **86**, 3602 (2001).
- [31] H. W. Streitwolf, *Phys. Rev. B* **58**, 14356 (1998).
- [32] S. Tretiak, A. Piryatinski, A. Saxena, R. L. Martin, and A. R. Bishop, *Phys. Rev. B* **70**, 233203 (2004).
- [33] C. Grebogi, S. M. Hammel, J. A. Yorke, and T. Sauer, *Phys. Rev. Lett.* **65**, 1527 (1990).
- [34] T. Sauer, C. Grebogi, and J. A. Yorke, *Phys. Rev. Lett.* **79**, 59 (1997).
- [35] R. W. Brankin, I. Gladwell, and L. F. Shampine, *RK-SUITE: a suite of Runge-Kutta codes for the initial value problem for ODEs* (Softreport 92-S1, Department of Mathematics, Southern Methodist University, Dallas, Texas, 1992), www.netlib.org.
- [36] K. A. Chao and Y. Wang, *J. Phys. C:Solid State Phys.* **18**, L1127 (1985).
- [37] M. Hillery, R. F. O’Connell, M. O. Scully, and E. P. Wigner, *Phys. Rep.* **106**, 121 (1984).

- [38] V. I. Tatarskii, *Sov. Phys. Usp.* **26**, 311 (1983).
- [39] X.-P. Jiang and P. Brumer., *Chem. Phys. Lett.* **208**, 179 (1993).
- [40] S. Adachi, V. M. Kobryanskii, and T. Kobayashi, *Phys. Rev. Lett.* **89**, 027401 (2002).
- [41] G. Lanzani, C. Cerullo, and N. S. Sariciftci, *Phys. Rev. Lett.* **90**, 047402 (2003).
- [42] H. Hwang and P. J. Rossky, *J. Phys. Chem. B* **108**, 6723 (2004).
- [43] M. F. Kling, C. Siedschlag, A. J. Verhoef, J. I. Khan, M. Schultze, T. Uphues, Y. Ni, M. Uiberacker, M. Drescher, F. Krausz, et al., *Science* **312**, 246 (2006).